

SCIENTIFIC REPORTS

OPEN

One-Step Hydrothermal Fabrication of Three-dimensional MoS₂ Nanoflower using Polypyrrole as Template for Efficient Hydrogen Evolution Reaction

Received: 10 October 2016
Accepted: 08 January 2017
Published: 14 February 2017

Xin Lu¹, Yingwu Lin^{1,2}, Haifeng Dong², Wenhao Dai², Xin Chen², Xuanhui Qu¹ & Xueji Zhang²

Herein, a facile and cost-effective strategy for hydrothermal synthesis of three-dimensional (3D) MoS₂ with adequate active edge sites and advanced hydrogen evolution reaction (HER) performance using polypyrrole (PPy) as template is reported. The MoS₂ is first thermally nucleated using hexaammonium heptamolybdate tetrahydrate (NH₄)₆Mo₇O₂₄·4H₂O and thiourea as precursor in the presence of PPy, and then they are further annealed to remove PPy at higher temperature to generate 3D MoS₂-P. Morphology and composition characterizations reveal that the 3D MoS₂-P exhibits a nanoflower morphology. It presents larger stretched “thin folding leaves” and higher mesoporous volume of 0.608 cm³ g⁻¹ than the MoS₂ without PPy as template. Importantly, the 3D MoS₂-P shows enhanced HER catalytic activity (onset potential at -100 mV) than previously reports that MoS₂-based HER catalysts. The large “thin folding leaves” possessing efficient edge active sites and defects are responsible to for the enhanced HER performance, while the high mesoporous volume facilitates the transfer of reaction substrate. Our study provides a facile and cost-effective method for synthesis of 3D MoS₂ with advanced HER performances, which has great potential for larger-scale production and practical industrial applications.

Hydrogen is a green and sustainable energy, acting as attractive alternative of traditional fossil fuels to alleviate the energy crisis and environmental pollution^{1,2}. Electrolytic water is an efficient and clean technology for hydrogen evolution³, and Pt-based noble metal electrocatalysts are commonly employed in hydrogen evolution reaction (HER) to improve the reaction efficiency. However, the high cost and rare reserve are still hinder its practical application⁴. Efficient alternatives are under urgent need. Recently, two dimensional layered molybdenum disulfide (MoS₂) based materials are emerging as the promising HER. It was supported by both theoretical calculations and experimental studies^{5,6}. Density function theory (DFT) calculation revealed that the thermodynamic free energy of H adsorption on the unsaturated sulfur atoms at MoS₂ edge sites was fit for HER application⁷. Additionally, its relatively low cost, abundant reserve and good stability make MoS₂ a promising alternative candidate of Pt in HER^{8,9}. However, the relatively lower catalytic activity of bulk MoS₂ compared to Pt trigger intense research that improve the catalytic capability¹⁰.

Generally, three strategies are employed to improve the catalytic properties of MoS₂. First, much effort has devoted to generation of defects to obtain more active edges per unit area, and thus more active sites. Advanced hydrothermal synthesis methods¹¹, including plasma-engineered^{12,13} or rough substrate chemical vapor deposition (CVD)¹⁴ are designed to generate defects for enhanced HER. Xie *et al.* developed a hydrothermal routine and paved the way of engineering defects into MoS₂ using high concentration of the precursors and different amounts of thiourea¹¹. The second strategy strives to strengthen the electrochemical properties by atomic-scale

¹Institute for Advanced Materials and Technology, University of Science & Technology Beijing, Beijing 100083, P.R. China. ²Beijing Key Laboratory for Bioengineering and Sensing Technology, Research Center for Bioengineering and Sensing Technology, School of Chemistry & Biological Engineering, University of Science & Technology Beijing, Beijing 100083, P.R. China. Correspondence and requests for materials should be addressed to H.D. (email: hfdong@ustb.edu.cn) or X.Z. (email: zhangxueji@ustb.edu.cn)

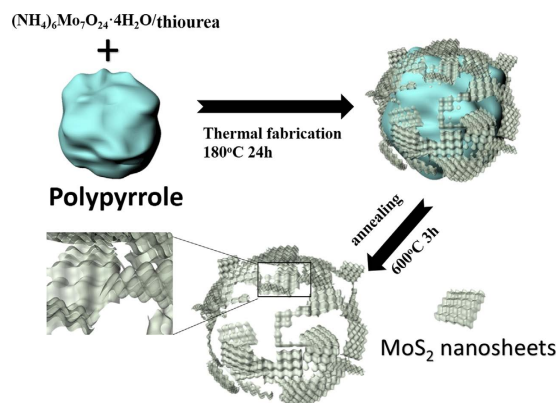


Figure 1. Schematic illustration of the morphological evolution process of the MoS₂-P.

modification including chemical doping¹⁵, adjustment of the metastable 1T-phase^{16,17} and strain treating¹⁸. Furthermore, fabrication of efficient 3D MoS₂ such as porous nanosheets¹⁹, vertical nanoflakes²⁰, core-shell MoO₃-MoS₂ nanowires^{21,22} and double-gyroid morphology²³ etc. are explored to increase specific surface area and active sites, leading to high catalytic activity. Zhang *et al.* designed an edge-rich and highly ordered MoS₂ nanosheets rooting into polyaniline nanofibers. It showed good catalytic properties and stability²¹. Kibsgaard *et al.* engineered the surface structure of MoS₂ to preferentially expose edge sites for improved catalytic activity by successfully synthesizing contiguous large-area thin films of a highly ordered double-gyroid MoS₂ with nanopores²³. Our group designed a 3D nitrogen-doped graphene supported MoS₂ as an advanced HER catalyst²⁴. Among them, various 3D MoS₂ structures with high-surface and exposed active sites present great prospect in large-scale and practical applications.

Although reasonable progresses have been achieved in fabrication of 3D structure, it still suffers from some deficiencies such as complicated operation with multiple steps and inefficient catalytic activity. It is highly desirable to develop a facile and straightforward approach to fabricate cost-effective MoS₂-based catalysts with high HER activity.

Herein, a one-step hydrothermal synthesis route for 3D MoS₂ flower with advanced HER performance using PPy (MoS₂-P) was developed. The PPy shows excellent conductivity. Specially, it displays good stability²⁴ to keep its morphology during the hydrothermal synthesis, which is good candidate for soft template. Moreover, it has been demonstrated that the molybdenum sulfide anions prefer to attach and dope into PPy, inducing formation of MoS₂ nanosheets on the surface of the PPy instead of forming independent nanoflowers²⁵. Comprehensive characterizations revealed a nanoflower morphology of the resulting MoS₂-P. It presented larger area “thin folding leaves” and much more mesoporous pore than the counterpart without PPy as template. Enhanced HER performance was demonstrated. The “thin folding leaves” possessed adequate edge active sites, enabling the enhanced HER performance. The higher mesoporous volume facilitates efficient transfer of reaction substrate. The PPy template could generate nanoflower morphology with larger stretched “thin folding leaves” and higher mesoporous volume as well as much more tortuous and cleaved lattice structures than the MoS₂ without PPy as template. By adjusting the concentration of the PPy, both the morphology and the defects can be controllably engineered. The proposed method is a facile and cost-effective, providing great potential for larger-scale production of 3D MoS₂ with advanced HER performances and practical industrial application.

Results

The one-step hydrothermal synthesis method is schematically illustrated in Fig. 1. (NH₄)₆Mo₇O₂₄·4H₂O and thiourea were chosen as the precursor for large-quantity of MoS₂ preparation in the presence of PPy. The PPy was employed as the template to generate a MoS₂ structure with large surface area and adequate active edges. The (NH₄)₆Mo₇O₂₄·4H₂O, thiourea and PPy were simultaneously transferred into the Teflon-lined stainless-steel autoclave for hydrothermal synthesis to generate MoS₂/PPy composite. The resulting composite was further annealed at higher temperature to remove the PPy^{24,26} to produce 3D MoS₂-P. The PPy played critical roles in the formation of unique morphology and electrochemical performance of the MoS₂-P, which will be addressed in the following section.

Scanning electron microscope (SEM) and transmission electron microscope (TEM) were employed to characterize the morphology of the synthesized composites. As shown in Fig. 2, in comparison with the MoS₂ without PPy as template displaying a compact nanoflower structure (Fig. 2b), the MoS₂-P presented a nanoflower morphology with larger stretched “thin folding leaves” (Fig. 2a). PPy acts as a soft template for MoS₂ in the experiments, providing a substrate to support the growth of MoS₂. Thus, the morphology of the PPy will influence the morphology of MoS₂-P. The SEM image (Fig. S1) shows that the morphology of PPy is an irregular sphere with rough surface, which provide a template for the formation of nanoflower of MoS₂-P (Fig. 2b). As shown in Fig. S2, the annealing process could effectively remove the PPy²⁴. The annealing process also induce tortuous and cleaved lattice in the MoS₂-P. The large “thin folding leaves” of the nanoflower structure possessing efficient edge active sites and defects are responsible to the enhanced HER performance. The decrease of carbon component during the annealing process further confirmed the effective removal of PPy (Fig. S3). TEM image confirms the larger stretched thin films of MoS₂-P (Fig. 2c) compared to the closed nanoflower of MoS₂ without PPy as template

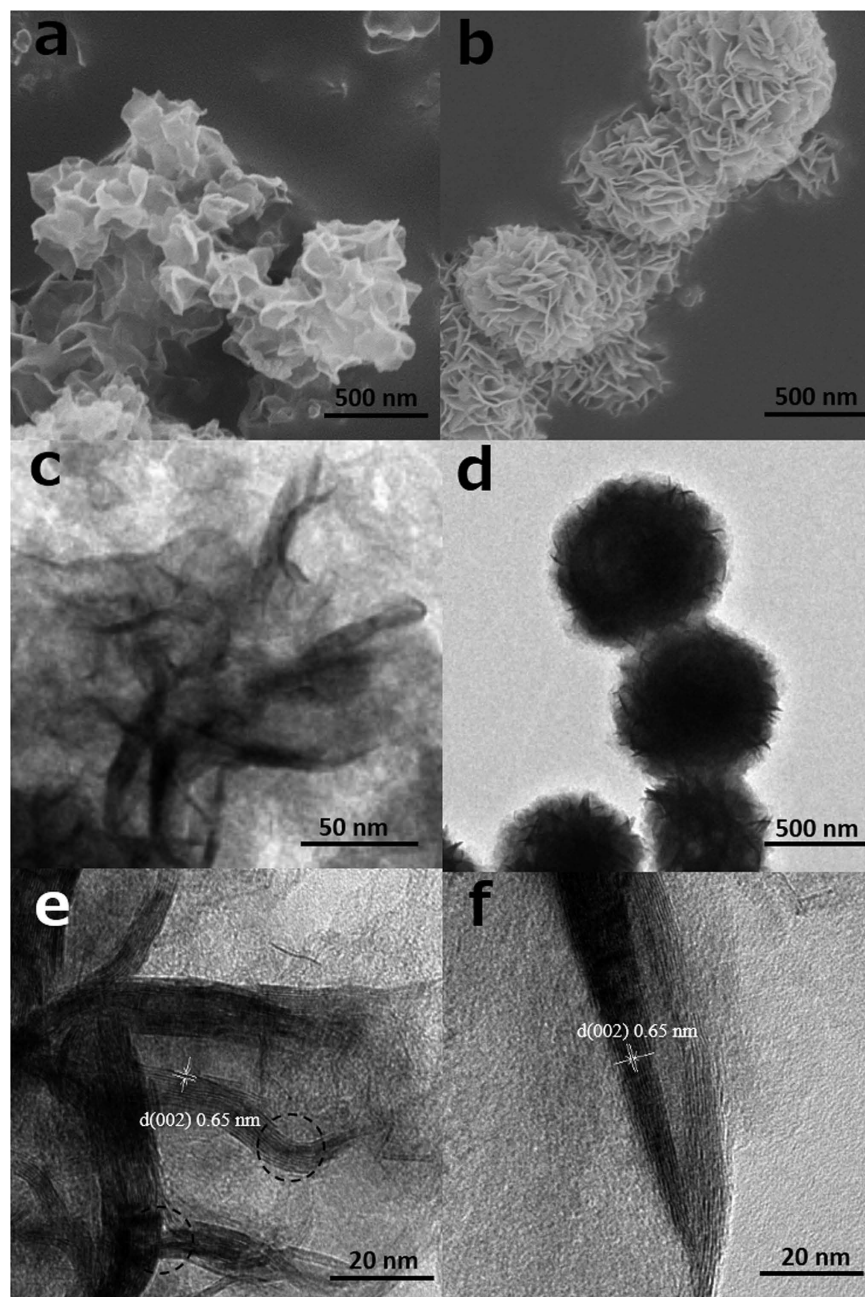


Figure 2. (a) SEM image of MoS₂-P; (b) SEM image of MoS₂; (c) TEM image of MoS₂-P; (d) TEM image of MoS₂; (e) HRTEM image of MoS₂-P; (f) HRTEM image of MoS₂.

(Fig. 2d). These results revealed that the PPy template effectively inhibited the aggregation of MoS₂ during hydrothermal synthesis process. The formation of stretched “thin folding leaves” is vital for HER, because the adequate exposure of active sites facilitate the efficient substrate accessibility compared to the MoS₂ that with lots of active edges hid inside the nanoflowers. The high-resolution TEM (HRTEM) image analysis of MoS₂-P displayed a clean lattice structure with an interplanar spacing of 0.65 nm (Fig. 2e) ascribed to the (002) planes of MoS₂¹¹, similar to the MoS₂ (Fig. 2f), which suggested that the MoS₂ was successfully synthesized. Importantly, numerous tortuous and cleaved lattice structures were observed in the MoS₂-P (circle in Fig. 2e), indicating the formation of numerous defects during the PPy-assisted MoS₂ hydrothermal synthesis.

As shown in Fig. 3a, both of the nitrogen (N₂) adsorption-desorption isotherms of the MoS₂ and MoS₂-P presented typical IV isotherms hysteresis loop associated with large size mesoporous. The H3 hysteresis loop of MoS₂-P and MoS₂ indicated the presence of slit nanopore²⁷. Brunauer–Emmett–Teller (BET) calculation revealed that MoS₂-P displayed six times larger surface area of 431.2 m² g^{−1} than that of MoS₂ (60.3 m² g^{−1}). Although MoS₂-P and MoS₂ displayed similar pore size of 19 nm, MoS₂-P showed a four-fold higher pore volume of 0.608 cm³ g^{−1} than that of MoS₂ with a pore volume of 0.156 cm³ g^{−1} (Fig. 3b). Thus, the PPy and annealing process rendered MoS₂-P with large surface area and adequate nanopores.

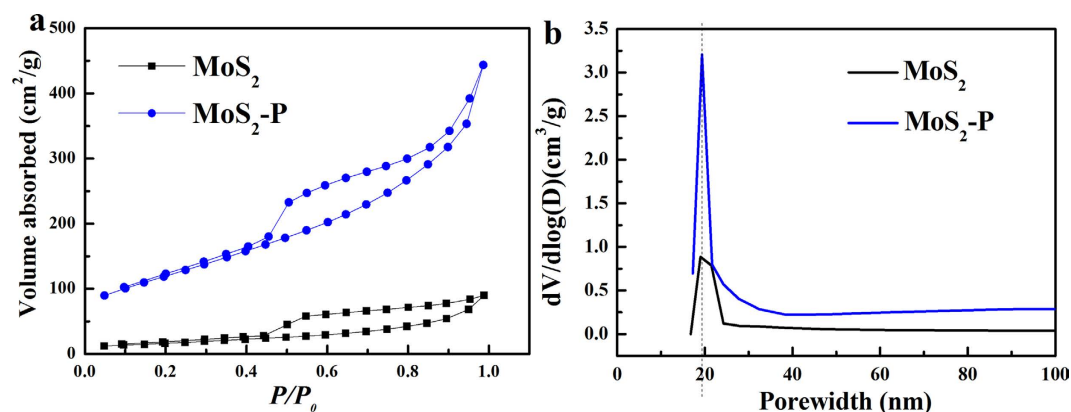


Figure 3. (a) Nitrogen adsorption-desorption characterizations of MoS₂-P (blue curve) and MoS₂ (black curve); (b) the pore size distribution of MoS₂-P (blue curve) and MoS₂ (black curve).

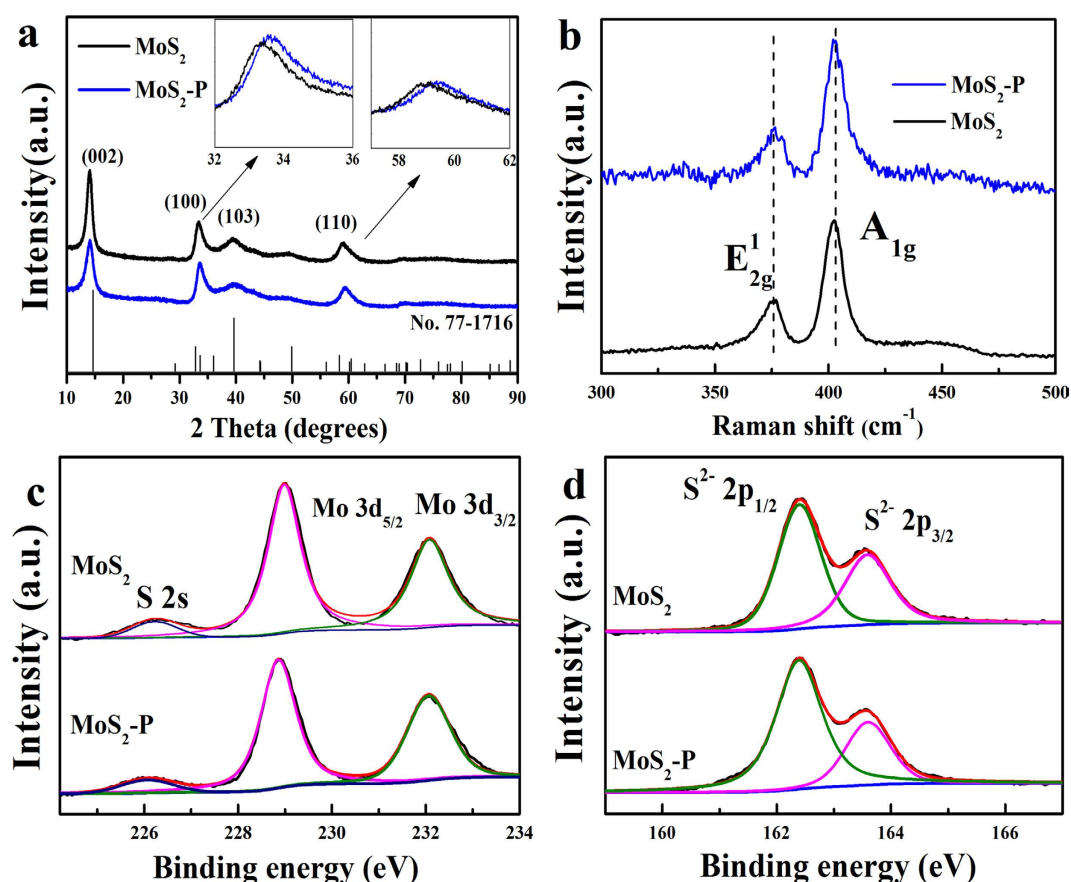


Figure 4. Characterization of MoS₂ and MoS₂-P by (a) XRD; (b) Raman spectroscopy and High-resolution (c) Mo 3d and (d) S 2p XPS spectra. Inset a: the magnified image of the (100) and (110) peak of the MoS₂ and MoS₂-P.

As shown in Fig. 4a, in agreement with MoS₂ (black curve), the characteristic peaks of MoS₂-P at $2\theta = 14.3, 33.6, 29.7, 59.0$ corresponding to the (002), (100), (103), (110) planes (blue curve). It confirmed the well defined and hexagonally symmetric structured of MoS₂ (JCPDS card no. 77-1716). It indicated less layers of MoS₂-P than MoS₂ according to Scherrer analysis of the half maximum (FWHM) value in the (002) diffraction peak¹⁷ (Fig. 4a). The slight shift of (100) and (110) between MoS₂ and MoS₂-P was resulted from the crystal lattice tortuosity ($\lambda = 2d\sin\theta$) (Fig. 4a, inset). The recovery of characteristic peaks in MoS₂-P compared to PPy encapsulated MoS₂ (PPy-MoS₂) (Fig. S4) as well as the thermogravimetric analysis curve of MoS₂-P (Fig. S5) proved the annealing process removed effectively the PPy. The two strong characteristic peaks located at 376 and 402 cm⁻¹ were ascribed to E_{2g}, A_{1g} respectively. It suggested the resulted MoS₂-P (Fig. 4b, blue curve) and MoS₂ (Fig. 4b,

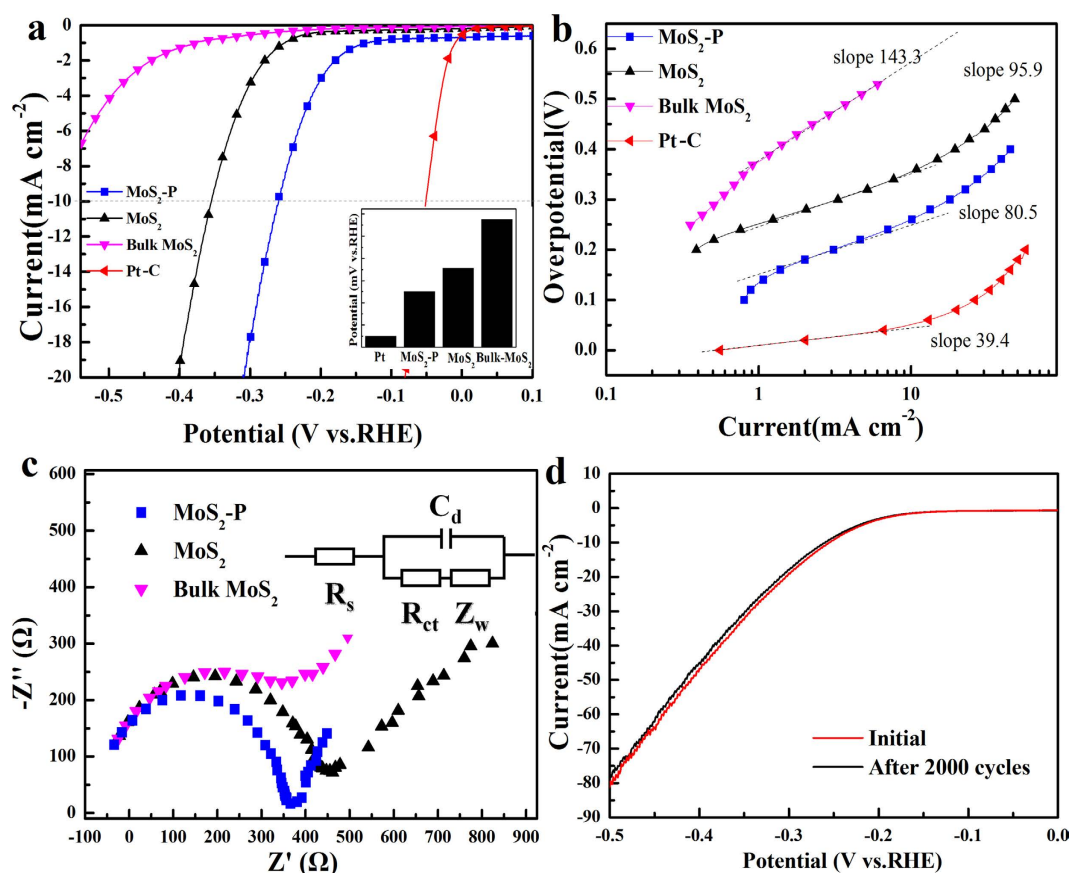


Figure 5. (a) Polarization curves obtained of catalysts as indicated; inset: the overpotential of catalysts when the current is 10 mA cm^{-2} . (b) Corresponding Tafel plots recorded on glassy carbon electrodes with a catalyst loading of 0.28 mg cm^{-2} . (c) Nyquist plots of the MoS_2 catalyst recorded. Inset c: equivalent circuit of the EIS spectroscopy. (d) Durability test showing negligible current loss even after 2000 cycles.

black curve) were mainly 2H- MoS_2 , and the slight red shift of A_{1g} in $\text{MoS}_2\text{-P}$ compared to MoS_2 was caused by the crystal lattice tortuosity²⁸.

The components of the MoS_2 samples were investigated by X-ray photoelectron spectroscopy (XPS). The MoS_2 and $\text{MoS}_2\text{-P}$ showed the characteristic peaks of the Mo 3d, S 2p and O 1s (Fig. S6). The appearance of weak N 1s peak located at 396 eV and slight increase of C 1s at 285.2 eV in $\text{MoS}_2\text{-P}$ (Fig. S6b) compared to MoS_2 (Fig. S6a) was resulted from carbonization remnants of PPy during the annealing process. It suggested that PPy might carbonized partially rather than decomposed completely, and it might also generated active nitrogen hybrid species for enhanced HER performance²⁴. As shown in the Mo 3d spectrum of $\text{MoS}_2\text{-P}$ (Fig. 4c, blue curve), the peak located at 229.8 and 232.9 eV is assigned to Mo 3d_{5/2} and Mo 3d_{3/2}, respectively^{29,30}, which further suggested the resulting $\text{MoS}_2\text{-P}$ was mainly consisted of 2H semiconducting structure¹⁶ (Fig. 4c, black curve). Similarly, the characteristic peaks of S 2p spectrum in $\text{MoS}_2\text{-P}$ (Fig. 4d, blue curve) at 162.4 and 163.5 eV attributed to S 2p_{3/2} and S 2p_{1/2} were presented (black curve), indicating the domain oxidation state of S²⁻³¹. The XPS analysis revealed that the $\text{MoS}_2\text{-P}$ and MoS_2 have little difference in elemental composition and bonding configuration. Similar to MoS_2 , the $\text{MoS}_2\text{-P}$ displayed a strong absorption 671 nm, and the band gap was calculated to be 1.52 eV (Fig. S6), agreeing with previous report³².

The HER electrochemical performance of the $\text{MoS}_2\text{-P}$ was further investigated. Figure 5a shows representative linear sweep voltammetry (LSV) response for the bulk MoS_2 , commercial Pt-C, MoS_2 and $\text{MoS}_2\text{-P}$. The MoS_2 exhibited superior HER performance (black curve) than the raw bulk MoS_2 (purple curve)¹¹. The $\text{MoS}_2\text{-P}$ (blue curve) displayed enhanced HER catalytic activity with negative onset overpotential of 100 mV than that of MoS_2 with an onset overpotential of 170 mV. The $\text{MoS}_2\text{-P}$ presented superior an overpotential of -251 mV for 10 mA cm^{-2} to the MoS_2 of 350 mV and bulk MoS_2 of 578 mV (Fig. 5a, inset). The $\text{MoS}_2\text{-P}$ displayed a smaller Tafel slope of 80.5 mV/dec (Fig. 5b, blue curve) than MoS_2 of 95.9 mV/dec (Fig. 5b, black curve) and bulk MoS_2 of 143.3 mV/dec (Fig. 5b, purple curve). These results confirmed the enhanced HER performance of $\text{MoS}_2\text{-P}$ than MoS_2 and bulk MoS_2 .

To obtain more information about the intrinsic catalytic activity, the turnover frequency (TOF) for the active sites of different MoS_2 catalysts was calculated using the roughness factor method according to the following equations³³.

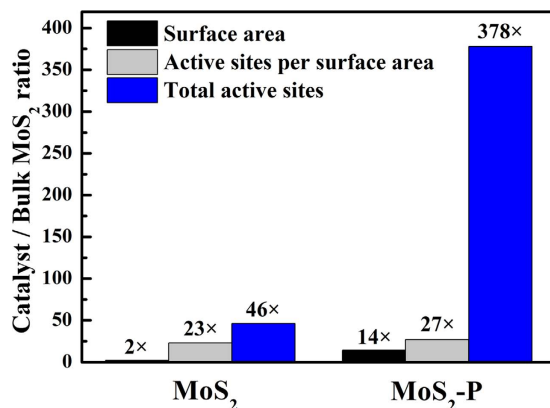


Figure 6. Ratios of surface area, active sites per surface area and total active sites of MoS₂ and MoS₂-P versus the bulk MoS₂.

$$D_c = D_s \times \frac{C_{dlc}}{C_{dls}} \quad (1)$$

$$\text{TOF}(s^{-1}) = \frac{j/(2 \times q)}{D_c} \quad (2)$$

where D_c and D_s were the density of active sites for catalyst (Sites/cm²) and standard sample (Sites/cm²), the C_{dls} and C_{dlc} were the double layer capacitor (C_{dl}) for standard MoS₂ (60 μF cm⁻¹) and catalysts calculated by the cyclic voltammetry (CV) experiment at different scan rates (Fig. S7), the j (A cm⁻²) was the current density of LSV at −400 mV and q was the elementary charge (1.6×10^{-19} C). The active sites density of MoS₂-P was 3.35×10^{17} sites/cm², 1.2 times and 27 times higher than that of MoS₂ (2.85×10^{17} sites/cm²) and that of bulk MoS₂ (1.24×10^{16} sites/cm²), respectively. The MoS₂-P presented enhanced TOF of $0.85 s^{-1}$ to MoS₂ ($0.67 s^{-1}$) and bulk MoS₂ ($0.54 s^{-1}$), further indicating advanced HER catalytic activity of MoS₂-P. Electrochemical impedance spectroscopy (EIS) was used to characterize the interfacial reaction and electron-transfer kinetics in HER. As shown in Fig. 5c, MoS₂-P displayed the lowest faradaic impedance and smallest charge transfer resistance (R_{ct}) among these MoS₂ catalysts. For the long-time durability, the MoS₂-P showed a negligible decrease in the current density after a long period of 2000 potential-cycling between 0 and −0.5 V, indicating the outstanding electrochemical stability and its promising potential for the practical application (Fig. 5d).

Briefly, the most important step involved in the HER process is the hydrogen adsorption, which require appropriate Gibbs free energy of the catalyst. Increasing theoretical and experimental reports confirmed the Gibbs free energy of H adsorption on the unsaturated atoms at MoS₂ edge active site are favorable to hydrogen adsorption, leading to the efficient hydrogen evolution⁷ (Fig. S8). We further compared the HER performance of the MoS₂-P to previous reports of MoS₂-based HER catalysts. As shown in Table S1, the MoS₂-P showed more competitive performance than most of the previous MoS₂-based catalyst. The enhanced HER performance could be explained as follows: First, the unique nanoflower morphology of large stretched “thin folding leaves” allowed considerable active site exposure for HER (Fig. 2a and c). The quantity of total active sites (calculated by the surface area multiply the density of active sites for catalyst (Sites/cm²)) for MoS₂-P is 8.2 times higher than that of MoS₂ and 378 times higher than that of bulk MoS₂ (Fig. 6). Secondly, the numerous defects resulted from the tortuous and cleaved lattice formed during the annealing process also contribute to enhance HER performance (Fig. 2e). Additionally, the high mesoporous volume of MoS₂-P facilitates the efficient mass transfer.

Discussion

In this study, we have developed a facile and cost-effective strategy for large-scale synthesis of 3D MoS₂ nanoflower with large stretched “thin folding leaves” and considerable nanopores by using a PPy-assisted one-step hydrothermal routine. Microscopic and spectroscopic tools including SEM, TEM, HRTEM, BET, XRD, XPS and Raman spectroscopy was employed to comprehensively characterize the morphology and component of the MoS₂-P. Electrochemical characterizations demonstrated that the prepared MoS₂-P displayed advanced HER performance. It presenting superior onset overpotential, Tafel plot and lower faradaic impedance than MoS₂ without using PPy as template, which was competitive to most of the reported analogous MoS₂-based catalyst. It also displayed long outstanding electrochemical stability for the practical application. It was demonstrated that the high quantity of exposed active sites on the large surface and the defects formed during the hydrothermal synthesis synergistically contribute to the advanced HER catalytic activity, while unique mesoporous structure facilitates the accessibility of the reacted substrate. The facile and cost-effective method for larger-scale synthesis 3D MoS₂ with advanced HER performances holds great promising in practical industrial application.

Methods

Materials and Reagents. $(\text{NH}_4)_6\text{Mo}_7\text{O}_{24}\cdot 4\text{H}_2\text{O}$, Polypyrrole (PPy, un-doped, extent of labeling: ~20 wt. % loading, composite with carbon black and the CAS number is 30604-81-0) and Pt/C (10% Pt) were obtained from Sigma-Aldrich. Thiourea and KOH were from Sinopharm Chemical Reagent Co., Ltd. Sulfuric acid (H_2SO_4 , 95–98%) and ethanol (99.9%) was purchased from Beijing Chemical Works. All aqueous solutions were prepared with ultrapure water obtained from a Millipore water purification system ($\geq 18\text{ M}\Omega$, Milli-Q, Millipore).

X-ray diffraction (XRD) was performed by a Rigaku X-ray diffractometer with Cu KR target. The porosity was measured with a nitrogen adsorption-desorption isotherm using a surface area analyzer (QuadraSorb SI 2000–08, Quantachrome Instruments). The morphologies of products were observed under a field-emission scanning electron microscope (SEM; HITACHI S-4800) and a transmission electron microscope (TEM; JEM-2010, 200 kV). X-ray photoelectron spectroscopy (XPS) analysis was performed using an AXIS ULTRADLD instrument equipped with an Al K α X-ray source. Raman spectra were recorded on an InVia-Reflex Raman microscope with a laser excitation wavelength of 532 nm.

Materials Preparation of MoS_2 and MoS_2 -P. MoS_2 -P were synthesized by a hydrothermal synthesis; typically, 44.8 mg polypyrrole (PPy), 123.625 mg hexaammonium heptamolybdate tetrahydrate (0.1 mmol, $(\text{NH}_4)_6\text{Mo}_7\text{O}_{24}\cdot 4\text{H}_2\text{O}$, i.e. 0.7 mmol Mo) and 228.375 mg thiourea (3 mmol) were dissolved in ultrapure water (20 mL) under vigorous stirring to form a homogeneous solution. Then, the solution was transferred into a 25 mL Teflon-lined stainless steel autoclave and maintained at 180 °C for 24 h, and the reaction system was then cooled to room temperature. The final product was washed thoroughly with water and ethanol to remove any possible ions, and the as-prepared hydrogel was directly dehydrated via a freeze-drying process to maintain the 3D monolithic architecture, and then annealed at 600 °C for 3 h under argon. As a control, the MoS_2 was prepared in a similar procedure except using PPy as template.

Electrochemical Characterization. Electrochemical measurements were performed using a CHI 852C electrochemical workstation (Shanghai Chenhua Instrument Co., China) with a standard three-electrode setup in 0.5 M H_2SO_4 aqueous solution. A saturated calomel electrode (Hg/HgCl $_2$ in saturated KCl) and a graphite rod were used as the reference electrode and the counter electrode, respectively. A glass carbon rotating ring-disk electrodes (RRDE) loading the catalyst was used as the working electrode. Experimentally, 1 mg of the respective catalyst powder was dispersed in 1 mL of ethanol with 50 μL of Nafion solution and ultrasonicated for 15 min. A 20 μL of the resulting solution was dropped onto the glassy-carbon disk (diameter of 3 mm) using a microliter syringe and dried at room temperature. The catalyst loadings were all 0.28 mg cm^{-2} . Linear sweep voltammetry (LSV) was performed in nitrogen-saturated 0.5 M H_2SO_4 at a scan rate of 10 mV s^{-1} at 1400 rpm. Electrochemical impedance spectroscopy (EIS) was measured in the same configuration from 10^{-2} to 10^6 Hz with modulation amplitude of 5 mV. SCE was calibrated to reversible hydrogen electrode (RHE). A Pt wire was used as the working electrode and the counter electrode, respectively, and the calibration was carried out in a high purity H_2 -saturated electrolyte at a scan rate of 0.1 mV s^{-1} . The potential at which the current crossed zero was taken to be the thermodynamic potential for the hydrogen electrode reactions. In 0.5 M H_2SO_4 , $E(\text{RHE}) = E(\text{SCE}) + 0.26\text{ V}$. All the potentials reported in our manuscript are against RHE.

References

1. Milliken, J. A., Josecka, F., Wang, M. & Yuzugulluc, E. The Advanced Energy Initiative. *J. Power. Sources*. **172**, 121–131 (2007).
2. Dresselhaus, M. S. & Thomas, I. L. Alternative Energy Technologies. *Nature*. **414**, 332–337 (2001).
3. Xu, S. *et al.* Semimetallic Molybdenum Disulfide Ultrathin Nanosheets as an Efficient Electrocatalyst for Hydrogen Evolution. *Nanoscale*. **6**, 8359–8367 (2014).
4. Petrik, L. F., Godongwana, Z. G. & Iwuoha, E. I. Platinum Nanophase Electro Catalysts and Composite Electrodes for Hydrogen Production. *J. Power. Sources*. **185**, 838–845 (2008).
5. Jaramillo, T. F. *et al.* Identification of Active Edge Sites for Electrochemical H_2 Evolution From MoS_2 Nanocatalysts. *Science*. **317**, 100–102 (2007).
6. Wang, Q. *et al.* Electronics and Optoelectronics of Two-Dimensional Transition Metal Dichalcogenides. *Nat. Nanotechnol.* **7**, 699–712 (2012).
7. Berit, H. *et al.* Biomimetic Hydrogen Evolution: MoS_2 Nanoparticles as Catalyst for Hydrogen Evolution. *J. Am. Chem. Soc.* **127**, 5308–5309 (2005).
8. Benck, J. D. *et al.* Catalyzing the Hydrogen Evolution Reaction (HER) with Molybdenum Sulfide Nanomaterials. *ACS Catal.* **4**, 3957–3971 (2014).
9. Merki, D. & Hu, X. Recent Developments of Molybdenum and Tungsten Sulfides as Hydrogen Evolution Catalysts. *Energy Environ. Sci.* **4**, 3878–3888 (2011).
10. Jaegermann, W. & Tributsch, H. Interfacial Properties of Semiconducting Transition Metal Chalcogenides. *Prog. Surf. Sci.* **29**, 1–167 (1988).
11. Xie, J. *et al.* Defect-Rich MoS_2 Ultrathin Nanosheets with Additional Active Edge Sites for Enhanced Electrocatalytic Hydrogen Evolution. *Adv. Mater.* **25**, 5807–5813 (2013).
12. Li, T. *et al.* Plasma-Engineered MoS_2 Thin-Film as an Efficient Electrocatalyst for Hydrogen Evolution Reaction. *Chem. Commun.* **51**, 7470–7473 (2015).
13. Islam, M. R. *et al.* Tuning the Electrical Property Via Defect Engineering of Single Layer MoS_2 by Oxygen Plasma. *Nanoscale*. **6**, 10033–10039 (2014).
14. Sina, N. *et al.* Synthesis and Defect Investigation of Two-Dimensional Molybdenum Disulfide Atomic Layers. *Accounts Chem. Res.* **48**, 31–40 (2014).
15. Wang, H. *et al.* Transition-Metal Doped Edge Sites in Vertically Aligned MoS_2 Catalysts for Enhanced Hydrogen Evolution. *Nano. Res.* **8**, 566–575 (2015).
16. Acerce, M., Voiry, D. & Chhowalla, M. Metallic 1T Phase MoS_2 Nanosheets as Supercapacitor Electrode Materials. *Nat. Nanotechnol.* **10**, 1–6 (2015).
17. Lukowski, M. A. *et al.* Enhanced Hydrogen Evolution Catalysis From Chemically Exfoliated Metallic MoS_2 Nanosheets. *J. Am. Chem. Soc.* **135**, 10274–10277 (2013).

18. Li, H. *et al.* Activating and Optimizing MoS₂ Basal Planes for Hydrogen Evolution through the Formation of Strained Sulphur Vacancies. *Nat. Mater.* **15**, 48–53 (2016).
19. Qi, J. *et al.* Porous Metallic MoO₂-supported MoS₂ Nanosheets for Enhanced Electrocatalytic Activity in the Hydrogen Evolution Reaction. *Nanoscale*. **7**, 5203–5208 (2015).
20. Kong, D. *et al.* Synthesis of MoS₂ and MoSe₂ Films with Vertically Aligned Layers. *Nano. Lett.* **13**, 1341–1347 (2013).
21. Zhang, N. *et al.* Edge-Rich MoS₂ Nanosheets Rooting Into Polyaniline Nanofibers as Effective Catalyst for Electrochemical Hydrogen Evolution. *Electrochim. Acta*. **180**, 155–163 (2015).
22. Nikam, R. D. *et al.* Three-Dimensional Heterostructures of MoS₂ Nanosheets on Conducting MoO₂ as an Efficient Electrocatalyst to Enhance Hydrogen Evolution Reaction. *ACS Appl. Mater. Inter.* **7**, 23328–23335 (2015).
23. Jakob, K., Zhebo, C., Reinecke, B. N. & Jaramillo, T. F. Engineering the Surface Structure of MoS₂ to Preferentially Expose Active Edge Sites for Electrocatalysis. *Nat. Mater.* **11**, 963–969 (2012).
24. Dong, H. *et al.* Three-Dimensional Nitrogen-Doped Graphene Supported Molybdenum Disulfide Nanoparticles as an Advanced Catalyst for Hydrogen Evolution Reaction. *Sci. Rep.* **5**, 17542–17552 (2015).
25. Wang, T., Zhuo, J., Du, K. *et al.* Electrochemically fabricated polypyrrole and MoS(x) copolymer films as a highly active hydrogen evolution electrocatalyst. *Adv. Mater.* **22**, 3761–6 (2014).
26. Wu, Z. S. *et al.* 3D Nitrogen-Doped Graphene Aerogel-Supported Fe₃O₄ Nanoparticles as Efficient Electrocatalysts for the Oxygen Reduction Reaction. *J. Am. Chem. Soc.* **134**, 9082–9085 (2012).
27. Lowell, S. *Characterization of Porous Solids and Powders: Surface Area, Pore Size and Density* (ed. Shields, J. E.) 130–132 (Springer Science & Business Media, 2012).
28. Jiménez, S. S., Yang, D., Frindt, R. F. & Irwin, J. C. Raman Study and Lattice Dynamics of Single Molecular Layers of MoS₂. *Phys. Rev. B*. **44**, 3955–3962 (1991).
29. Ge, X. *et al.* Nanoporous Metal Enhanced Catalytic Activities of Amorphous Molybdenum Sulfide for High-Efficiency Hydrogen Production. *Adv. Mater.* **26**, 3100–3104 (2014).
30. Liao, L. *et al.* MoS₂ Formed On Mesoporous Graphene as a Highly Active Catalyst for Hydrogen Evolution. *Adv. Funct. Mater.* **23**, 5326–5333 (2013).
31. Yuan, H., Li, J., Yuan, C. *et al.* Facile Synthesis of MoS₂@CNT as an Effective Catalyst for Hydrogen Production in Microbial Electrolysis Cells. *Chemelectrochem.* **1**, 1828–1833 (2014).
32. Mak, K. F., Lee, C., Hone, J. *et al.* Atomically thin MoS₂: a new direct-gap semiconductor. *Phys. Rev. Lett.* **105**, 136805 (2010).
33. Behranginia, A. *et al.* Highly Efficient Hydrogen Evolution Reaction Using Crystalline Layered Three-Dimensional Molybdenum Disulfides Grown on Graphene Film. *Chem. Mater.* **28**, 549–555 (2016).

Acknowledgements

The work was supported by National Natural Science Foundation of China (Grant No. 21305008, 21475008), and Ph.D. Programs Foundation of Ministry of Education of China (No. 11170197), the Fundamental Research Funds for the Central Universities (NO. FRF-BR-15-020A); State Key Laboratory of Analytical Chemistry for Life Science SKLACLS1401.

Author Contributions

X.L., Y.L. and H.D. conceived the project and designed the experiment; Y.L. synthesized the material; W.D., X.C. and Y.L. performed the microscopic and spectroscopic study; Y.L. and X.L. performed the electrochemistry experiments; X.L., Y.L. and H.D. analyzed the data and wrote the main manuscript text; X.Q., W.D. and X.Z. modified the manuscript. All authors have given approval to the final version of the manuscript.

Additional Information

Supplementary information accompanies this paper at <http://www.nature.com/srep>

Competing financial interests: The authors declare no competing financial interests.

How to cite this article: Lu, X. *et al.* One-Step Hydrothermal Fabrication of Three-dimensional MoS₂ Nanoflower using Polypyrrole as Template for Efficient Hydrogen Evolution Reaction. *Sci. Rep.* **7**, 42309; doi: 10.1038/srep42309 (2017).

Publisher's note: Springer Nature remains neutral with regard to jurisdictional claims in published maps and institutional affiliations.



This work is licensed under a Creative Commons Attribution 4.0 International License. The images or other third party material in this article are included in the article's Creative Commons license, unless indicated otherwise in the credit line; if the material is not included under the Creative Commons license, users will need to obtain permission from the license holder to reproduce the material. To view a copy of this license, visit <http://creativecommons.org/licenses/by/4.0/>

© The Author(s) 2017